Materials Horizons

ROYAL SOCIETY OF CHEMISTRY

COMMUNICATION

Published on 25 June 2026
Licence and permissions

Cite this: *Mater. Horiz.*, 2026, **13**, 8002

Received 11th April 2026,
Accepted 15th June 2026

DOI: 10.1039/d6mh00722h

rsc.li/materials-horizons

Bio-inspired micro-architected mechanochromic materials with radiative signature modulation

Stefanos Mavrikos,†[a] Nikolina Nikolarea,†[bc] Dimitrios E. Manolakos[b] and Costas P. Grigoropoulos *[a]

Drawing inspiration from the panther chameleon's sophisticated color-adaptive abilities, we introduce a unified design framework for a new class of bio-inspired mechanochromic materials with tailored reflectivity across the electromagnetic spectrum. While structural coloration in nature relies on the mechanical adjustment of photonic crystal spacing, engineering such systems is often hindered by the barreling effect, the lateral bulging of bulk materials caused by Poisson's effect. To address this, we developed a mechanical metamaterial substrate optimized through a genetic algorithm and modeled it using Timoshenko beam theory to ensure a uniform strain field during deformation. The proposed system features a two-dimensional hexagonal lattice of composite dielectric nanopillars positioned on top of a micro-architected substrate fabricated *via* Multiphoton Lithography (MPL). The nanopillars consist of an MPL core coated with a high-refractive-index material to achieve complete optical band gaps. By dynamically adjusting the lattice constant through controlled, reversible elastic deformation, the reflected wavelengths can be shifted across broad spectral ranges. We demonstrate the scalability and robustness of this approach through three distinct structures tailored for the visible, mid-wave infrared (MWIR), and long-wave infrared (LWIR) regions. This methodology lays a foundation for scalable, reversible mechanochromic materials with significant potential for applications in adaptive camouflage, radiative thermal management, and wearable electronics.

New concepts

This work shifts the paradigm of mechanochromic design from chemistry-dependent pigments to a purely architectural approach, where optical functionality is a programmable property of the material's structural geometry. The core innovation lies in solving the barreling effect, *i.e.*, the lateral bulging of the material in response to loading, by introducing a mechanical metamaterial substrate optimized through a genetic algorithm (GA). This GA-driven method allows for precise customization of individual beam stiffnesses, maintaining a uniform strain field that preserves the periodicity of the photonic lattice during deformation. Additionally, by incorporating Timoshenko beam theory into the design of sub-micron lattices fabricated *via* Multiphoton Lithography (MPL), we bridge the gap between structural mechanics and high-resolution additive manufacturing. This integrated framework offers a "tunable-by-design" scalable approach that extends beyond the visible spectrum, providing a reliable method to engineer reversible radiative signatures in the mid-wave and long-wave infrared regions, capabilities previously limited by material properties or fabrication constraints.

Introduction

The effort to design and create artificial mechanochromic materials that can undergo dynamic, reversible color changes in response to external mechanical stimuli has long been inspired by the sophisticated color-adaptive strategies found in nature.[1] This remarkable ability of natural organisms to control their color arises from two main mechanisms:[2] pigmentary mechanochromism, in which color changes result from the material's chemical composition and mechanically induced variations, and structural mechanochromism, wherein color arises from how light interacts with nano- or microstructured surfaces. The latter is common in nature, as many organisms have iridophores on their surfaces, and their spatial rearrangement can alter the parts of the optical spectrum they engage with, creating the so-called "play of colors".[3–5] One of the most well-known examples is the chameleon, whose dermal iridophores enable rapid, reversible shifts in skin reflectance by mechanically adjusting the spacing of intracellular guanine nanocrystals.[6] These nanocrystals form a periodic photonic lattice, and strain-induced changes in their lattice spacing cause broad-spectrum optical shifts in a highly energy-efficient manner. When mechanical strain is applied, the spacing between the nanocrystals shifts, thereby altering the

[a] *Department of Mechanical Engineering, University of California, Berkeley, CA, 94720, USA. E-mail: cgrigoro@berkeley.edu*
[b] *School of Mechanical Engineering, National Technical University of Athens, 15780, Greece*
[c] *Department of Mechanical Engineering, Johns Hopkins University, Baltimore, MD, 21218, USA*
† These authors contributed equally to this work.

optical band gap. Applying this elegant principle of structural coloration to engineered systems offers a groundbreaking way to develop materials with tunable optical properties. Such advancements have important implications for a range of applications, including adaptive camouflage, radiative thermal management, wearable electronics, and strain-based mechanical sensing.

Numerous research efforts have been made to develop color-changing materials responsive to mechanical inputs, utilizing mechanically induced chemical changes to produce color shifts under varying stresses or strains.[7–19] The main limitations of these materials are the requirement for an external voltage source, their narrow spectral shift capabilities, and their lack of scalability due to reliance on the chemistry of specific pigments, which limits their optical shifting capabilities in the visible spectrum. Conversely, approaches inspired by natural structural coloration have yielded static, non-tunable designs.[20–23] Mechanical metamaterials could serve as an alternative platform for creating dynamic, color-changing structures; however, such designs are often complex and challenging to fabricate using traditional manufacturing methods, making additive manufacturing the only practical solution.[24,25] In fact, an additively manufactured structure with tunable radio-frequency absorbance has been proposed, but it is not scalable for visible or infrared spectra, as the resolution and feature sizes achievable with the employed manufacturing technique are limited.[26]

Multiphoton lithography (MPL) is an additive manufacturing method that relies on the local polymerization of a negative-tone photoresist *via* multiphoton absorption.[27,28] MPL offers extremely high resolution, far below the diffraction limit of the light source used, because it depends on the simultaneous nonlinear absorption of multiple (usually two) photons from an ultrafast laser to locally solidify a volume element called a voxel.[29] Since its first demonstration in the late 1990s by Maruo, Nakamura, and Kawata,[30] it has gained significant attention from the research community due to its extensive design flexibility and manufacturing capabilities, such as creating smooth freeform surfaces[31] and complex structures on various substrates,[32] which are not achievable with traditional $2\frac{1}{2}$-dimensional photolithography methods. The versatility of MPL has been demonstrated across numerous applications, including micro-optics,[33] microfluidics,[34] notable advances in Lab-on-a-Chip technologies,[35] microelectromechanical systems (MEMS),[36] and biomedical and tissue engineering.[37] Beyond these fields, MPL has almost revolutionized the development of mechanical metamaterials, enabling the fabrication of complex micro-architected materials with programmable,[38] exceptional mechanical properties, such as auxetic[39] and impact-resistant structures.[40]

Considering the challenges of designing bio-inspired materials with tunable optical properties and the advanced manufacturing capabilities offered by MPL, developing materials with adjustable absorptivity across the optical and infrared spectra is achievable. A new class of mechanochromic materials, intended for fabrication *via* MPL, can be introduced. Their optical properties can be tuned by shifting the optical bandgap and, consequently, the reflected wavelengths, through changes in the photonic crystal's lattice constant. However, using bulk material as a substrate for the photonic crystal is impractical because creating a uniform strain field is impossible due to Poisson's effect and the corresponding barreling effect, the lateral bulging of the material in response to mechanical loading.[41,42] Therefore, a mechanical metamaterial with controlled barreling effect that adjusts its Poisson ratio in different directions must be designed. The entire process should account for MPL's manufacturing capabilities and limitations, specifically factors such as resolution and feature size, as well as the properties of the available material palette, to propose a feasible, manufacturable design.

Nonetheless, local distortions in the photonic crystal will occur due to unavoidable small inhomogeneities in deformation and manufacturing. The impact of these imperfections on the crystal's optical properties should be assessed to determine the design's effectiveness and robustness. Additionally, since the color change must be reversible, the lattice must stay stable and only deform elastically, avoiding any permanent deformation.

In this work, we introduce an integrated design workflow for chameleon-skin-inspired mechanochromic materials with tunable reflectivity across the visible and infrared regions of the electromagnetic spectrum, which can be fabricated using MPL. The process begins with calculating the optical band gaps of a hexagonal crystal array through wave-propagation analyses that treat the problem as an eigenvalue problem. The photonic crystals are designed to be two-dimensional and composed of composite dielectric rods in air. For a specific region of the electromagnetic spectrum, the photonic crystal is initialized, and a lattice serving as the substrate is designed so that its deformation under lateral load distorts the crystal, enabling a gradually shifting spectrum of reflected light. The lattice design combines classical beam theory with a genetic algorithm to achieve a uniform strain field. This design framework is applied to three structures with tailored reflectivity in the visible, mid-wave infrared, and long-wave infrared regions of the electromagnetic spectrum, respectively, demonstrating the feasibility and scalability of the proposed bio-inspired approach.

Results

Bio-inspired design of the photonic crystal

The panther chameleon (Furcifer pardalis) is a reptile native to Madagascar whose ability for dynamic reversible color change has attracted researchers' interest.[6] This remarkable ability results from the outer layer of its skin acting as a natural photonic crystal. Guanine nanocrystals, which have a high refractive index, are organized in a hexagonal lattice within the cytoplasm, a material with a low refractive index, as shown in Fig. 1A. This transition from high to low refractive index produces a photonic crystal with specific optical band gaps, which are ranges of light frequencies that cannot pass through

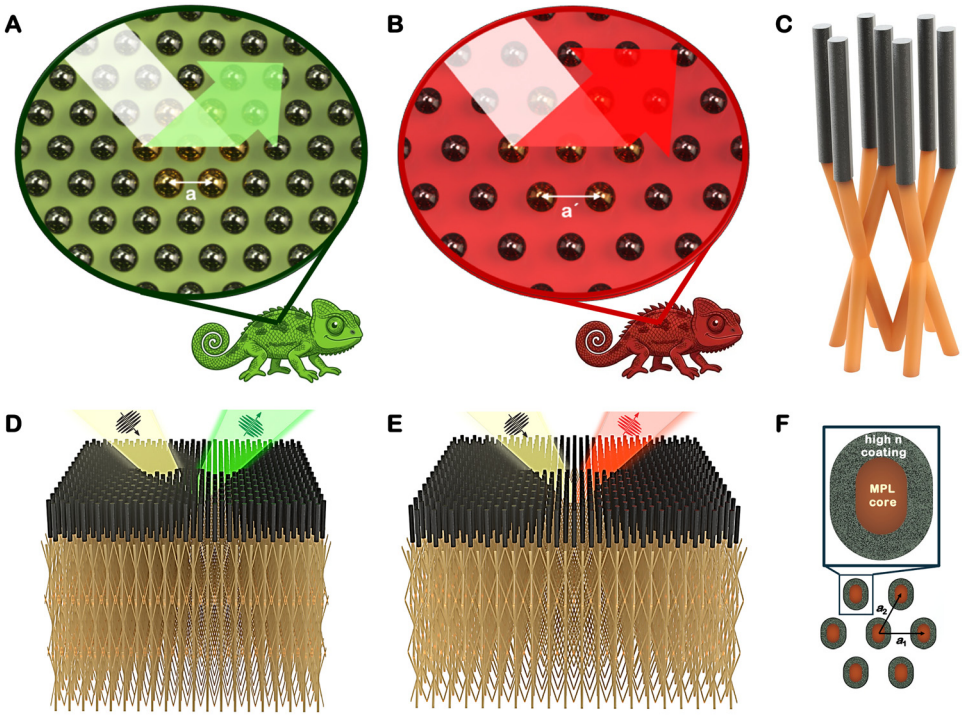

Fig. 1 Chameleon-skin-inspired mechanochromic material with tailored radiation signature. (A) Chameleons' skin consists of guanine nanocrystals, which have a high refractive index in the visible spectrum, arranged in a hexagonal array within the cytoplasm, a material with a lower refractive index in the same spectrum. The formed photonic crystal exhibits optical band gaps proportional to the lattice constant, a, thereby blocking the propagation of a specific part of the spectrum, which is reflected and gives the animal its color. (B) When the skin stretches, the lattice constant changes, making $a' > a$, and a different part of the incident white light is reflected, changing the animal's color. (C) The bio-inspired two-dimensional photonic crystal consists of dielectric nanorods positioned on a mechanical metamaterial fabricated *via* Multiphoton Lithography (MPL). (D) Drawing inspiration from the natural color-change mechanism, the design of structures with tailored reflectivity in a specific regime of the visible or infrared spectrum is feasible. (E) The reflected wavelengths can be dynamically and reversibly shifted, resulting in structures capable of altering their "color" across different parts of the electromagnetic spectrum. (F) The proposed photonic crystal consisted of MPL-fabricated nanorods coated with a high-refractive-index material in the targeted spectral regime.

the material and are reflected, appearing as color. By physiological movements, the chameleon's skin deforms, changing the lattice geometry and shifting the crystal's optical bandgap. For example, the skin can be stretched by bending the back, increasing the distance between the guanine nanocrystals, thereby shifting the crystal's optical bandgap and reflecting longer wavelengths, thereby changing the chameleon's color, as shown in Fig. 1A and B. It is important to note that stretching only alters the lattice constant and not its shape, leaving the nanocrystal hexagonal arrangement unchanged.

Drawing inspiration from this natural mechanism, a design for a two-dimensional photonic crystal composed of dielectric nanopillars has been developed (Fig. 1D). This design features a complete band gap, meaning that electromagnetic waves within a certain wavelength range cannot propagate through the structure for either transverse electric (TE) or transverse magnetic (TM) modes, allowing unpolarized light to be reflected and visible to the naked eye.[43,44] This principle can be generalized and applied to the design of materials with tailored, tunable infrared reflectivity. Consequently, structures capable of reflecting different parts of the infrared spectrum by dynamically altering the spacing between dielectric rods, as demonstrated in Fig. 1D and E, can be designed. Complete band gaps are not achievable with dielectric circular rods in common lattices such as the square and hexagonal lattices.[45,46] It has been discovered that hexagonal lattices display complete band gaps when the dielectric rods have elliptical cross-sections, and are composite with a core and outer shell made of different materials.[47] Therefore, we designed hexagonal lattices with dielectric rods as composite nanopillars with a discorectangle cross-section, shown in Fig. 1E, featuring a core made from the same resin as the metamaterial substrate, fabricated *via* MPL, and an outer coating of a high-refractive-index material.

Three different structures were designed to demonstrate the scalability of our method. All structures were compressed to a maximum nominal strain of 5.2% to prevent structural instabilities, such as buckling and plastic deformation, thereby ensuring the reversible nature of the proposed design. The reflected electromagnetic spectrum shifted from 511 nm to 493 nm for the first structure, from 5.36 μm to 5.25 μm for the second, and from 11.24 μm to 10.99 μm for the third, as shown in Fig. 2. For each design, the band diagrams for both the relaxed and the maximum-strained states are presented, along with changes in the band gaps of the different structures as the nominal strain progressively increases. It is important to note that the optical response, in the case of an incident beam with a broad

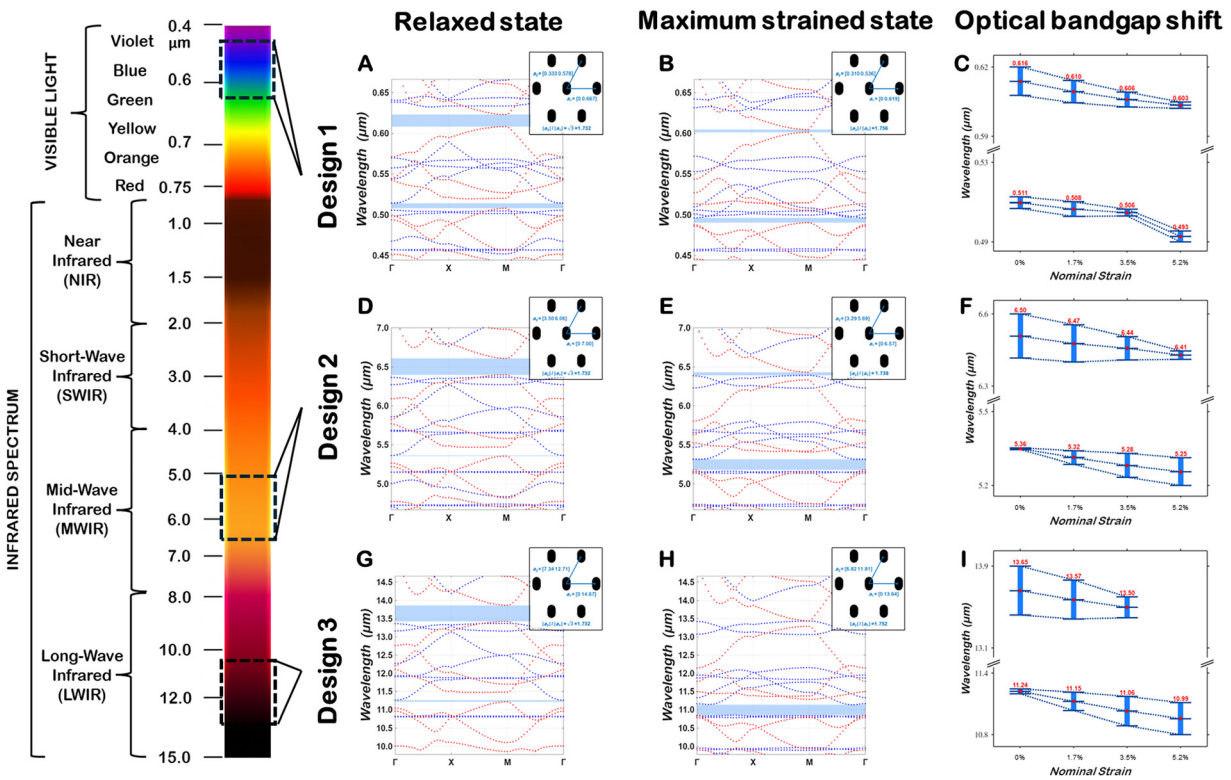

Fig. 2 The introduced framework is applied to the design of three different structures with tailored reflectivity in different spectral regimes. Under externally applied strain, the optical band gaps can be shifted. (A–C). Design 1 can alter its reflectivity in the "blue" part of the visible spectrum. (D–F). Design 2 can alter its reflectivity in the mid-wave infrared spectrum. (G–I). Design 3 can alter its reflectivity in the long-wave infrared spectrum (in band diagrams: TM modes in blue and TE modes in red).

spectrum, such as a white light source in the visible spectrum, can be a combination of different band gaps, where the shifting and the width of each one contribute to the overall reflectivity of the designed photonic crystal. For example, in Fig. 2, the behavior of two band gaps is displayed as each metamaterial deforms. This enables more intense irradiation-shifting phenomena.

Design of the mechanical metamaterial

The substrate supporting the photonic crystal is a mechanical metamaterial that allows uniform deformation of the hexagonal nanopillar array, which is essential for the photonic crystal's optical response. Inspired by the Body Centered Cubic (BCC) unit cell and breaking its symmetry in the horizontal plane, with an aspect ratio of $1:\sqrt{3}$, we designed a unit cell that, when repeated in a three-dimensional scaffold, can support the hexagonal photonic crystal on its top layer of nodes, as shown in Fig. 3A. The shorter dimension corresponds to the periodicity of the photonic crystal. The relative height of the unit cell is not strictly defined or limited by the physics of our problem, but we aimed to limit the unit cell's density, resulting in an aspect ratio of $1:\sqrt{3}:3$ in the XYZ frame of Fig. 3A.

The mechanical metamaterial is analytically modeled as a lattice composed of beam elements rather than axially loaded rods, because bending plays a significant role in the metamaterial's deformation. To create smaller structures with lower periodic constants, the beams have a relatively low length-to-thickness ratio. To account for this and ensure our model's accuracy, the behavior of each beam was calculated using Timoshenko beam theory instead of the more traditional Euler–Bernoulli beam theory.[48–51] Therefore, a closed-form analytical model for calculating lattice deformation is developed. Its accuracy is validated by comparing its results with experimental data to determine whether the model can predict the deformation of a structure fabricated *via* MPL with sub-micron features, as it is discussed in the SI.

To that end, using our analytical model, we simulated the compression test of four micro-lattices composed of different unit cells and calculated their Young's Moduli. The computed moduli were then compared with the experimental values obtained under uniform compressive loading using *in situ* SEM nanoindentation. The micro-lattices examined included four different unit cells that share many similarities with the proposed one. The average relative error in calculating the Young's Moduli is 2%. The low value of this error confirms that the analytical model accurately predicts the elastic deformation of MPL-fabricated micro-lattices and can be effectively integrated into the design process for the micro-architected substrate of the photonic crystal.

In our application, one side of the substrate is fixed, while the opposite side is subjected to uniform compression at a top

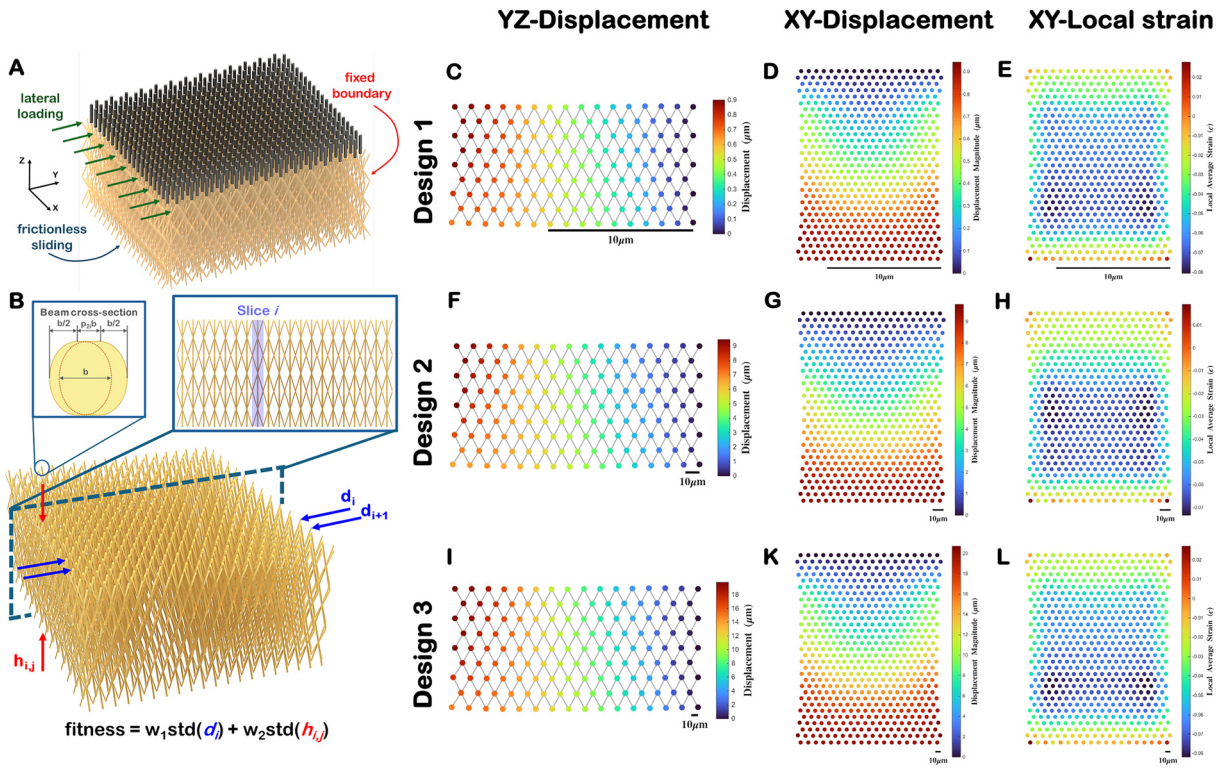

Fig. 3 Design of the mechanical material and calculation of its response under lateral loading. (A) The micro-architected material acts as the substrate for the photonic crystal and is loaded on the top edge of one of its vertical surfaces, allowing the lattice constant of the photonic crystal to be dynamically changed. The opposite face is fixed, while the remaining nodes are free. Under these boundary conditions, the mechanical response of the metamaterial is calculated using Timoshenko beam theory. (B) To reduce the barreling effect in the mechanical metamaterial, a genetic algorithm is used to properly control the stiffness of each beam, directing higher loads to stiffer beams. (C–E) The calculated displacement of the nodes on the mid-plane parallel to the YZ-plane and of the top surface, where the nanorods are located, along with the related local strain field for design 1. (F)–(H) The calculated displacement of the nodes on the mid-plane parallel to the YZ-plane and of the top surface, where the nanorods are located, along with the associated local strain field for design 2. (I)–(L) The calculated displacement of the nodes on the mid-plane parallel to the YZ-plane and of the top surface, where the nanorods are located, along with the corresponding local strain field for design 3.

edge, and the remaining nodes are free (Fig. 3A). To minimize the barreling effect and keep the photonic crystal as periodic as possible during compression, the metamaterial's beam stiffness should not be identical throughout the structure. The beam stiffness can be tuned in two different ways: by changing the beam inertia through varying the cross-sectional dimensions, and by altering the Young's Modulus of the polymerized photoresist. The second option is only possible thanks to MPL's powerful grayscale additive manufacturing capabilities. In light-based three-dimensional printing, the exposure dose dominates the material properties of the photocured material, as they are governed by the degree of convergence. The effectiveness of crosslinking, as a function of the number of absorbed photons, results in differentiated properties, including the Young's Modulus. By correlating the fabrication process parameters with the resulting Young's Modulus (reference me), the exposure dose can be appropriately varied during fabrication, yielding a lattice structure wherein each beam has a different Young's Modulus.

A simple genetic algorithm (GA) was used to determine the cross-sectional dimensions of each beam and the resin's Young's Modulus, since the elastic properties of the MPL-photopolymerized resin are influenced by fabrication settings. The GA setup is shown in Fig. 3B. For simplicity and ease of fabrication, each vertical "slice" of unit cells along the loading direction consists of identical beams. The global voxel size is initially set as an ellipsoid with an aspect ratio of 1 : 1 : 3, along with an initial Young's modulus. Then, the GA adjusts three design variables per slice in the initial equation. These variables relate to the settings used during MPL fabrication and the resulting beam cross-section.

This process varies the relative stiffness of each vertical slice. The decision to increase the cross-sectional area through multiple passes and to raise the Young's Modulus was made to achieve the high relative stiffness some slices needed, to reduce the barreling effect of the metamaterial. Both parameters have upper limits; the cross-sectional dimensions are limited to prevent excessive crowding inside the metamaterial, while the Young's Modulus of the resin cannot physically exceed 3.5 GPa.[52] The GA fitness function is the weighted sum of the standard deviation of the deformed structure's width along the loading direction and the standard deviation of the top nodes' height. Minimizing this function ensures the periodicity of the top nodes during deformation, resulting in a uniform strain field on the top surface of the metamaterial, on which the

dielectric rods are built, and the parallelism of the rods, preventing vertical lattice shelling.

Another factor considered during the design process is the structural instability caused by beam buckling. In this context, Euler's buckling load was calculated and compared to the maximum compressive load in the metamaterial to prevent such instabilities. The analytical calculations are discussed in (SI). The nominal compressive strain of the substrate, calculated from the overall lattice metamaterial dimensions, was set to at least 5.2% to ensure sufficient wavelength shift. At this strain, it was necessary for the ratio of maximum compressive load to the critical buckling load to stay below 0.85 throughout deformation. The strain of each beam was also calculated to confirm that the substrate deforms elastically, maintaining the reversibility of optical properties changes. It was concluded that the elasticity criterion was less restrictive than the buckling criterion. None of the beams' compressive strains exceeded 1.5%, while our resin studies indicate elastic behavior up to 2.6% strain. In the design process, the influence of the cyclical loading on the reversible nature of the structures was not considered, as no significant changes in the mechanical performance of structures fabricated by the employed photoresist were observed due to fatigue-related phenomena.[53]

Evaluation and robustness of the design process

The use of GA effectively reduces the barreling effect during deformation and minimizes strains and compressive stresses in the beams by distributing higher loads to the stiffer beams. As a result, the metamaterial can bear a global compressive strain of up to 5.2% while still satisfying the buckling criterion. To evaluate small distortions in the photonic crystal, we calculated the horizontal and vertical distances between each node and its top and right neighbors, capturing both normal and shear displacements. The distribution of computed displacements and strains across the metamaterial is presented in Fig. 3C–L. It is concluded that displacements, especially lateral ones, are larger near the edges of the metamaterial substrate, while a substantial region near the center of the top surface, as it is indicated in Fig. 4, remains sufficiently periodic, maintaining the hexagonal arrangement of the dielectric rods. The standard deviations of these displacements do not exceed 1.5% at maximum compressive strain. Only nodes within this area are used for constructing dielectric rods on top. These deviations are considered in the supercell simulation throughout the design process, as discussed in the SI, and serve as a criterion for determining whether the GA has achieved a satisfactory

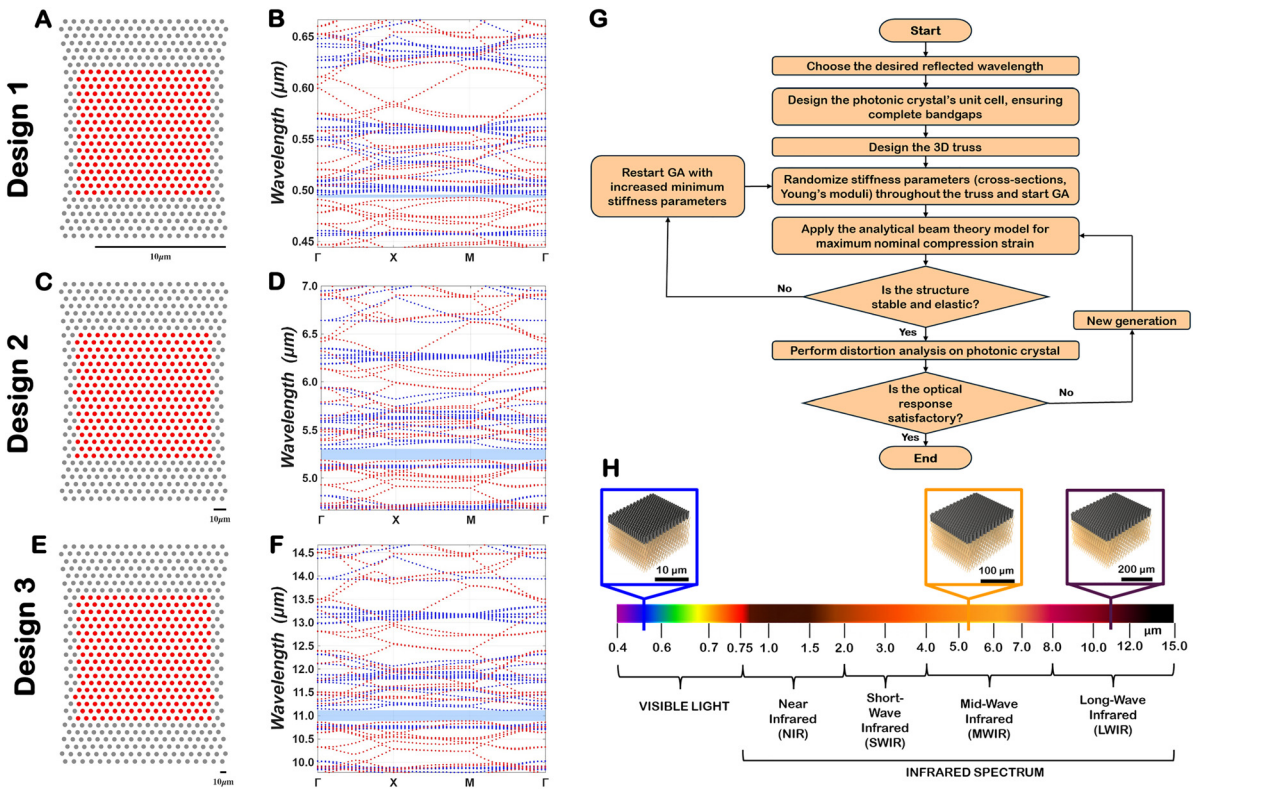

Fig. 4 The effect of geometrical distortions on the optical response of the designed photonic crystal and the overall "image" of the proposed unified design framework. (A) The actual area of the mechanical material (in red) where the geometric distortions are decided as sufficiently small, and, (B) the corresponding band diagram for design 1. (C) The actual area of the mechanical material (in red) where the geometric distortions are decided as sufficiently small, and, (D) the corresponding band diagram for design 2. (E) The actual area of the mechanical material (in red) where the geometric distortions are decided as sufficiently small, and, (F) the corresponding band diagram for design 3. (G) The introduced design framework is presented as a workflow. (H) The scalability of the proposed framework is demonstrated through its application across three distinct spectral regimes (visible, mid-wave and long-wave infrared). (in band diagrams: TM modes in blue and TE modes in red).

substrate design. The computed band gaps, accounting for distortions, are shown in Fig. 4.

Research indicates that as few as 25 dielectric rods are needed to replicate the results of an infinitely large photonic crystal.[54] Consequently, a hexagonal lattice of approximately 300 rods was considered sufficient for this proof-of-concept. Furthermore, two-dimensional photonic crystal simulations typically assume infinite length. In practice, this condition is met when the height of the dielectric rods is at least three times the wavelength that is expected to be reflected.[55]

Our study highlights the potential of structurally driven mechanochromism as a practical alternative to pigment-based methods, enabling tunable, scalable, and reversible designs and proposing a unified design framework presented as a workflow in Fig. 4G. Drawing inspiration from nature, our work shows that mechanical deformation of photonic crystals can produce significant, controllable optical shifts across a broad range of the electromagnetic spectrum (Fig. 4H).

Our analytical truss model demonstrates the scalability of the proposed design framework, needing only minor adjustments to beam sizes to balance axial and bending forces at different sizes. A key point is the relationship between mechanical performance and optical functionality. While the analytical three-dimensional truss model provides precise control over deformation, the requirement for uniform strain imposes strict design constraints on the metamaterial substrate. The optimization process effectively reduces barreling effects; however, some inhomogeneities remain unavoidable due to geometric constraints and manufacturing tolerances. Including the remaining distortions in an optical supercell simulation was essential for a more realistic performance assessment. Our results suggest that the photonic response of the structure is robust against small inhomogeneities. Ultimately, our findings are promising and will guide future experimental work.

Conclusion

Our work introduces a unified design approach for bio-inspired mechanochromic materials that combines photonic crystal engineering with mechanical metamaterial design within the manufacturing constraints of Multiphoton Lithography (MPL). By mimicking the structural coloration of animals such as the Panther chameleon, we demonstrate that tunable optical responses can be achieved through controlled deformation of mechanical structures.

The key contribution of this work is the development of an analytical three-dimensional truss model that facilitates the design of mechanical metamaterial lattices serving as substrates for photonic crystals. The model allows both tunable deformation and scalable structure, enabling the designer to systematically adjust the unit cell size for targeting different regions of the electromagnetic spectrum. Optimizing the stiffness parameters across the metamaterial and performing optical analysis with a supercell ensures that minor inhomogeneities within the deformed photonic crystal do not diminish its wavelength-shifting capabilities. Overall, the methodology presented establishes a foundation for a new class of scalable, mechanochromic materials with tailored radiative signatures poised for experimental validation. These materials potentially offer applications in adaptive optics, wearable devices, and advanced camouflage technologies. On-going research is currently focused on the fabrication and experimental demonstration of the herein proposed adaptive mechanochromic material.

Materials and methods

Photonic crystal simulations

Electromagnetic wave propagation simulations are performed using the COMSOL Multiphysics Wave Optics module to analyze the electromagnetic properties of the photonic crystals and generate the corresponding band diagrams. The photonic crystals are modeled as two-dimensional structures with Floquet-periodic boundary conditions. The structure is parameterized to accommodate different length scales and easily define deformations. The two larger structures, related to the infrared spectrum, feature a germanium (Ge) coating around the photopolymerized resin cores of the dielectric rods, as Ge has the highest refractive index in this spectral region.[56] The coating thicknesses were set to 440 nm and 920 nm, respectively. For the visible spectrum, both Ge and Gallium Arsenide (GaAs) can be used, with Ge's refractive index peaking at higher wavelengths (590 nm) than GaAs (428 nm).[57] This suggests that GaAs is more suitable for maintaining photonic band gaps across a wider range of the visible spectrum, whereas Ge might be better suited for color-changing structures that reflect wavelengths at the longer-wavelength end of the visible spectrum. The GaAs coating thickness was set equal to 44 nm.

Analytical truss model

The developed model is implemented as a MATLAB script and directly applies the three-dimensional Timoshenko beam theory, assuming a 12×12 stiffness tensor for each beam. Since the beams are fabricated *via* MPL with an ellipsoidal voxel aspect ratio of 1 : 1 : 3, as confirmed by SEM inspection of related structures, their cross-sections are elliptical, with the minor axis matching the voxel's and the major axis depending on the beam's orientation in space. The analytical expressions and the formulation of the developed model are discussed in depth in the SI.

Genetic algorithm

The GA population is 8 individuals, and it converges after 5 epochs. The fitness function is the weighted sum of three parameters: (a) $p_{i,1}$, a Boolean parameter (0 or 1) indicating whether the beams are fabricated with a single pass, resulting in an elliptical cross-section, or multiple passes to form a thicker, barrel-shaped cross-section; (b) $p_{i,2}$, a parameter (0.2, 0.4, or 0.6) representing the thickness of the beams in this slice if multiple passes are chosen, expressed as a fraction of the

voxel's minor axis length; and (c) $p_{i,3}$, a parameter (1, 1.25, 1.5 or 2) indicating how much higher the resin's Young's Modulus will be compared to the initial value of 1.2 GPa, which can be controlled by the process parameters during fabrication *via* MPL. The different values of the Young's Modulus were arbitrarily selected. Moreover, the resulting truss is independent of the initial value of the Young's Modulus, as follows from the equations of the analytical truss model.

Material in multiphoton lithography

In our study, the MPL material is SZ2080, a hybrid organic–inorganic resin that exhibits minimal shrinkage and residual strains and stresses during polymerization and development.[58,59] Its Young's Modulus has been measured experimentally to range from 0.6 GPa to 3.5 GPa, depending on process parameters such as laser intensity and scanning speed during MPL.[52,60]

Author contributions

Stefanos Mavrikos: conceptualization, data curation, formal analysis, investigation, methodology, resources, software, validation, visualization, writing – original draft; Nikolina Nikolarea: conceptualization, data curation, formal analysis, investigation, methodology, software, validation, visualization, writing – original draft; Dimitrios E. Manolakos: supervision, writing – review & editing; Costas P. Grigoropoulos: funding acquisition, project administration, resources, supervision, writing – review & editing.

Conflicts of interest

There are no conflicts to declare.

Data availability

The data supporting this article have been included as part of the supplementary information (SI). Supplementary information is available. See DOI: https://doi.org/10.1039/d6mh00722h.

Acknowledgements

S. M. would like to acknowledge and thank the Foundation for Education and European Culture for its financial support. N. N. would like to acknowledge and thank Mr Konstantinos Delimaris of the Photonics Initiative at ASRC CUNY for fruitful discussions. Support for this work by the US National Science Foundation under grants 2134534 and 2124826 is gratefully acknowledged. The research project was also supported by the Stavros Niarchos Foundation (SNF) and the Hellenic Foundation for Research and Innovation (H. F. R. I.) under the 5th call of ''Science and Society'' Action-''Always Strive for Excellence – Theodore Papazoglou'' (9578).

References

1 B. Bhushan, *Biomimetics: bioinspired hierarchical-structured surfaces for Green Science and Technology*, Springer, Cham, 3rd edn, 2018.
2 A. Lakhtakia and R. J. Martín-Palma, *Engineered biomimicry*, Elsevier, Amsterdam, 2013.
3 S. M. Doucet and M. G. Meadows, *J. R. Soc., Interface*, 2009, S115–S132.
4 L. Nahmad-Rohen, Y. H. Qureshi and M. Vorobyev, *Vision*, 2022, **6**, 59.
5 D. Gur, A. S. Moore, R. Deis, S. Pang, X. Wu, I. Pinkas, C. Deo, N. Iyer, H. F. Hess, J. A. Hammer and J. Lippincott-Schwartz, *Proc. Natl. Acad. Sci. U. S. A.*, 2024, **121**, e2308531121.
6 J. Teyssier, S. V. Saenko, D. Van Der Marel and M. C. Milinkovitch, *Nat. Commun.*, 2015, **6**, 6368.
7 H. Liu, X. Zhao, X. Yang, Y. Wang, M. Wu, J. Jiang, G. Wu, K. Yuan, L. Sui and B. Zou, *Nanoscale Horiz.*, 2020, **5**, 1233–1239.
8 M. Andrzejewski and A. Katrusiak, *J. Phys. Chem. Lett.*, 2017, **8**, 279–284.
9 P. Canasa, D. King, P. Cifligu, A. F. Lua Sanchez, S. L. Chen, H. Han, T. Malik, B. Billinghurst, J. Zhao, C. Park, G. R. Rossman, M. Pravica, P. K. Bhowmik and E. Evlyukhin, *Small Sci.*, 2024, **4**, 2400106.
10 Y. Sagara, T. Mutai, I. Yoshikawa and K. Araki, *J. Am. Chem. Soc.*, 2007, **129**, 1520–1521.
11 Y. Dong, J. Zhang, X. Tan, L. Wang, J. Chen, B. Li, L. Ye, B. Xu, B. Zou and W. Tian, *J. Mater. Chem. C*, 2013, **1**, 7554.
12 A. Seeboth, D. Loetzsch and R. Ruhmann, *Am. J. Mater. Sci.*, 2012, **1**, 139–142.
13 B. Fang, M. Chu, Z. Wu, Y. Shi, Y. S. Zhao and M. Yin, *J. Mater. Chem. C*, 2019, **7**, 4434–4440.
14 T. Suzuki, H. Okada, T. Nakagawa, K. Komatsu, C. Fujimoto, H. Kagi and Y. Matsuo, *Chem. Sci.*, 2018, **9**, 475–482.
15 Y. Chen, S. Wang, X. Wu, Y. Xu, H. Li, Y. Liu, H. Tong and L. Wang, *J. Mater. Chem. C*, 2018, **6**, 12503–12508.
16 Y. Li, Q. Fan, X. Wang, G. Liu, L. Chai, L. Zhou, J. Shao and Y. Yin, *Adv. Funct. Mater.*, 2021, **31**, 2010746.
17 N. Li, H. Liu, Y. Fang, L. Zhang, L. Sui, K. Yuan, G. Wu, K. Wang, B. Yang and B. Zou, *Appl. Phys. Lett.*, 2022, **121**, 111901.
18 C. Li, J. Liu, X. Qiu, X. Yang, X. Huang and X. Zhang, *Angew. Chem., Int. Ed.*, 2023, **62**, e202313971.
19 P. Liu, X. Ren, X. Qiu, X. Yang, Y. Wang and X. Zhang, *Macromolecules*, 2025, **58**, 6897–6906.
20 Y. Zhang, P. Han, H. Zhou, N. Wu, Y. Wei, X. Yao, J. Zhou and Y. Song, *Adv. Funct. Mater.*, 2018, **28**, 1802585.
21 L. Torres, J. L. Daristotle, O. B. Ayyub, B. M. Bellato Meinhardt, H. Garimella, A. Margaronis, S. Seifert, N. M. Bedford, T. J. Woehl and P. Kofinas, *Nanoscale*, 2019, **11**, 17904–17912.
22 G. H. Lee, J. B. Kim, T. M. Choi, J. M. Lee and S. Kim, *Small*, 2019, **15**, 1804548.
23 L. Shang, W. Zhang, K. Xu and Y. Zhao, *Mater. Horiz.*, 2019, **6**, 945–958.

24 H. Cui, D. Yao, R. Hensleigh, H. Lu, A. Calderon, Z. Xu, S. Davaria, Z. Wang, P. Mercier, P. Tarazaga and X. (Rayne) Zheng, *Science*, 2022, **376**, 1287–1293.

25 H. M. A. Kolken and A. A. Zadpoor, *RSC Adv.*, 2017, **7**, 5111–5129.

26 D. D. Lim, A. Ibarra, J. Lee, J. Jung, W. Choi and G. X. Gu, *Sci. Adv.*, 2025, **11**, eads3499.

27 M. Farsari and B. N. Chichkov, *Nat. Photonics*, 2009, **3**, 450–452.

28 G. Zyla and M. Farsari, *Laser Photonics Rev.*, 2024, **18**, 2301312.

29 V. Hahn, F. Mayer, M. Thiel and M. Wegener, *Opt. Photonics News*, 2019, **30**, 28.

30 S. Maruo, O. Nakamura and S. Kawata, *Opt. Lett.*, 1997, **22**, 132.

31 G. Zyla, G. Maconi, A. Nolvi, J. Marx, D. Ladika, A. Salmi, V. Melissinaki, I. Kassamakov and M. Farsari, *Light Adv. Manuf.*, 2024, **5**, 1.

32 M. Power, A. J. Thompson, S. Anastasova and G. Yang, *Small*, 2018, **14**, 1703964.

33 D. Gonzalez-Hernandez, S. Varapnickas, A. Bertoncini, C. Liberale and M. Malinauskas, *Adv. Opt. Mater.*, 2023, **11**, 2201701.

34 A. El-Tamer, U. Hinze and B. N. Chichkov, in *Handbook of Laser Micro- and Nano-Engineering*, ed K. Sugioka, Springer International Publishing, Cham, 2021, pp. 1691–1735.

35 F. Larramendy, S. Yoshida, D. Maier, Z. Fekete, S. Takeuchi and O. Paul, *Lab Chip*, 2019, **19**, 875–884.

36 H.-B. Sun and S. Kawata, in *NMR 3D Analysis Photopolymerization*, Springer Berlin Heidelberg, Berlin, Heidelberg, 2006, vol. 170, pp. 169–273.

37 V. Melissinaki, A. A. Gill, I. Ortega, M. Vamvakaki, A. Ranella, J. W. Haycock, C. Fotakis, M. Farsari and F. Claeyssens, *Biofabrication*, 2011, **3**, 045005.

38 L. V. Elliott, E. E. Salzman and J. R. Greer, *Adv. Funct. Mater.*, 2021, **31**, 2008380.

39 I. Spanos, Z. Vangelatos, C. Grigoropoulos and M. Farsari, *Nanomaterials*, 2021, **11**, 446.

40 C. M. Portela, B. W. Edwards, D. Veysset, Y. Sun, K. A. Nelson, D. M. Kochmann and J. R. Greer, *Nat. Mater.*, 2021, 1–7.

41 X. Wang, H. Li, K. Chandrashekhara, S. A. Rummel, S. Lekakh, D. C. Van Aken and R. J. O'Malley, *J. Mater. Process. Technol.*, 2017, **243**, 465–473.

42 T. W. Clyne and J. E. Campbell, *Testing of the Plastic Deformation of Metals*, Cambridge University Press, 1st edn, 2021.

43 J. D. Joannopoulos, S. G. Johnson, J. N. Winn and R. D. Meade, *Photonic Crystals: Molding the Flow of Light*, 2nd edn, Princeton University Press, 2008.

44 K. Sakoda, *Optical Properties of Photonic Crystals*, Springer Berlin, Heidelberg, 2005.

45 C. M. Anderson and K. P. Giapis, *Phys. Rev. Lett.*, 1996, **77**, 2949–2952.

46 Y. Kalra and R. Sinha, *Pramana*, 2008, **70**, 153–161.

47 T. Pan, F. Zhuang and Z.-Y. Li, *Solid State Commun.*, 2004, **129**, 501–506.

48 S. P. Timoshenko and Lond Edinb, *Dublin Philos. Mag. J. Sci.*, 1921, **41**, 744–746.

49 J. M. Gere and S. Timoshenko, *Mechanics of materials*, PWS-Kent Pub. Co, Boston, 3rd edn, 1990.

50 G. R. Cowper, *J. Appl. Mech.*, 1966, **33**(2), 335–340.

51 L. Andersen and S. R. Nielsen, *Aalb. Univ.*, 2008, **97**, 36.

52 L. Pertoldi, V. Zega, C. Comi and R. Osellame, *J. Appl. Phys.*, 2020, **128**, 175102.

53 E. Barchiesi, S. Mavrikos, I. Giorgio, C. Grigoropoulos, M. Farsari, F. Dell'isola and G. Zyla, *Contin. Mech. Thermodyn.*, 2024, **36**, 1755–1766.

54 A. Della Villa, S. Enoch, G. Tayeb, V. Pierro, V. Galdi and F. Capolino, *Phys. Rev. Lett.*, 2005, **94**, 183903.

55 M. Kafesaki, M. Agio and C. M. Soukoulis, *J. Opt. Soc. Am. B*, 2002, **19**, 2232–2240.

56 T. Amotchkina, M. Trubetskov, D. Hahner and V. Pervak, *Appl. Opt.*, 2020, **59**, A40.

57 K. Papatryfonos, T. Angelova, A. Brimont, B. Reid, S. Guldin, P. R. Smith, M. Tang, K. Li, A. J. Seeds, H. Liu and D. R. Selviah, *AIP Adv.*, 2021, **11**, 025327.

58 A. Ovsianikov, J. Viertl, B. Chichkov, M. Oubaha, B. MacCraith, I. Sakellari, A. Giakoumaki, D. Gray, M. Vamvakaki, M. Farsari and C. Fotakis, *ACS Nano*, 2008, **2**, 2257–2262.

59 A. I. Aristov, M. Manousidaki, A. Danilov, K. Terzaki, C. Fotakis, M. Farsari and A. V. Kabashin, *Sci. Rep.*, 2016, **6**, 25380.

60 G. Flamourakis, I. Spanos, Z. Vangelatos, P. Manganas, L. Papadimitriou, C. Grigoropoulos, A. Ranella and M. Farsari, *Macromol. Mater. Eng.*, 2020, **305**, 2000238.

